Available online at www.sciencedirect.com

SciVerse ScienceDirect

Neuromuscular Disorders 23 (2013) 84–88

www.elsevier.com/locate/nmd

Respiratory dysfunction in patients severely affected by GNE myopathy (distal myopathy with rimmed vacuoles)

Madoka Mori-Yoshimura [a,*], Yasushi Oya [a], Yukiko K. Hayashi [b,c], Satoru Noguchi [b], Ichizo Nishino [b,c], Miho Murata [a]

[a] *Department of Neurology, National Center Hospital, National Center of Neurology and Psychiatry, 4-1-1 Ogawahigashi, Kodaira, Tokyo 187-8551, Japan*

[b] *Department of Neuromuscular Research, National Institute of Neuroscience, National Center of Neurology and Psychiatry, 4-1-1 Ogawahigashi, Kodaira, Tokyo 187-8502, Japan*

[c] *Translational Medical Center, National Center of Neurology and Psychiatry, 4-1-1 Ogawahigashi, Kodaira, Tokyo 187-8502, Japan*

Received 28 March 2012; received in revised form 23 July 2012; accepted 25 September 2012

Abstract

GNE myopathy is a rare and mildly progressive autosomal recessive myopathy caused by *GNE* mutations. Respiratory dysfunction has not been reported in GNE myopathy patients. In this study, we retrospectively reviewed the respiratory function of 39 severely affected GNE myopathy patients (13 men, 26 women) from medical records, and compared these parameters with various other patient characteristics (e.g., *GNE* mutations, age at onset, creatine kinase levels, and being wheelchair-bound) for correlations. The mean % forced vital capacity [FVC] was 92 (26) (range, 16–128). In 12/39 (31%) patients, %FVC was <80%. Of these 12 patients, 11 (92%) were entirely wheelchair-dependent. These patients exhibited significantly earlier onset (20 [4] vs. 30 [8] years, $p < 0.001$) and lower creatine kinase levels (56 [71] vs. 279 [185] IU/L) than patients with normal respiratory function. Two patients exhibited severe respiratory failure and required non-invasive positive pressure ventilation. Patients with a homozygous mutation in the *N*-acetylmannosamine kinase domain exhibited lower %FVC, while only one compound heterozygous patient with separate mutations in the uridinediphosphate-*N*-acetylglucosamine 2-epimerase and the *N*-acetylmannosamine kinase domains had respiratory dysfunction. Our results collectively suggest that GNE myopathy can cause severe respiratory failure. Respiratory dysfunction should be carefully monitored in patients with advanced GNE myopathy characterized by early onset and homozygous homozygous mutations in the *N*-acetylmannosamine kinase domain.

Keywords: GNE myopathy; Distal myopathy with rimmed vacuoles (DMRV); Hereditary inclusion body myopathy; Respiratory dysfunction; Uridinediphosphate-*N*-acetylglucosamine (UDP-GlcNAc) 2-epimerase domain; *N*-acetylmannosamine kinase domain

1. Introduction

GNE myopathy, also known as distal myopathy with rimmed vacuoles (DMRV), Nonaka myopathy, or hereditary inclusion body myopathy (hIBM), is an early adult-onset, slowly progressive myopathy that preferentially affects the tibialis anterior muscle but relatively spares the quadriceps femoris muscles [1,2]. Respiratory dysfunction has not been reported in GNE myopathy [3]. Nonaka et al. reported that respiratory muscles were rarely involved even in bed-ridden patients, but no data were presented [1]. However, we had noticed that a few patients with GNE myopathy exhibited mild but progressive respiratory loss, with some experiencing recurrent pneumonia due to reduced airway clearance. Recent recommendations suggest training patients with neuromuscular disease with respiratory dysfunction using the air stacking technique to increase their thorax capacity and assisted cough peak flow (CPF) from an early stage to maintain lung compliance and chest mobility, and to clean the airways [4]. If respiratory dysfunction is not rare in patients with GNE

* Corresponding author. Tel.: +81 341 2711; fax: +81 342 1852.
E-mail address: yoshimur@ncnp.go.jp (M. Mori-Yoshimura).

0960-8966/$ - see front matter © 2012 Elsevier B.V. All rights reserved.
http://dx.doi.org/10.1016/j.nmd.2012.09.007

myopathy, then, physicians should punctually monitor their respiratory function with pulmonary function tests to look for early signs of respiratory dysfunction, perform respiratory training, coup with airway infection using a mechanical in-exsufflator (MI-E), and induce mechanical ventilation if required, as they do for patients with neuromuscular disease who exhibit respiratory failure.

The aim of this study is to evaluate past and present clinical respiratory function test parameters of GNE myopathy patients, and analyze factors that correlate with disease severity.

2. Patients and methods

2.1. Study population

Medical records of all genetically confirmed GNE myopathy patients who underwent pulmonary function tests at the National Center Hospital, National Center of Neurology and Psychiatry, were retrospectively reviewed. We collected data on genetic diagnosis, respiratory function (% vital capacity [%VC], % force vital capacity [FVC], cough peak flow [CPF]), creatine kinase (CK), chest X-ray and/or CT scan and body mass index (BMI) for analysis.

2.2. Data handling and analysis

Data were summarized using descriptive statistics, and each variable was compared against age, sex, respiratory dysfunction (whether their %FVC was up to or over 80%), and domain mutation (i.e., within the UDP-GlcNAc 2-epimerase domain: ED or *N*-acetylmannosamine kinase domain: KD). The *t*-test was used to compare the means of each group. Data for the two study populations were calculated using chi-square contingency table analysis. Multivariate regression analysis was performed with %FVC as the dependent variable. Explanatory variables included age at disease onset, CK and BMI. We found that the variables age, duration from onset to present, age upon wheelchair use, age at loss of ambulation, were highly correlated (over 0.5) with age at disease onset. As such, we eliminated these three due to multicolinearity in the multivariate regression analysis. When past %FVC data were available, the present data were compared with serial changes in respiratory function during the preceding 5–7 years, and changes in %FVC over time were determined by calculating the difference between past and present data. All analyses were performed using SPSS for Macintosh (Version 18; SPSS Inc., Chicago, IL).

3. Results

3.1. General characteristics

A total of 39 Japanese patients (13 men, 26 women) were recruited. The mean age at the time of data collection was 43.1 (11.3) years (mean [standard deviation, SD]) (Table 1). The mean age at first appearance of symptoms was 26.8 (9.0) years (range, 15–58 years; median, 25 years). Present age, age at disease onset, age at wheelchair use, and present ambulation status were not significantly different between men and women; 20.5% (8/39) had symptom onset before age 20. Of the 39 patients, 51.3% (20/39) could walk but needed assistance, and 69.2% (27/39) were wheelchair-bound (8/27 and 19/27 were partially and totally wheelchair-bound, respectively). Age at first use of a wheelchair was 33.3 (10.8) years (range, 18–59 years; median, 31.5 years) and that for loss of ambulation was 36.9 (11.9) years (Table 1).

3.2. GNE mutations

Of the 39 patients, 30.7% (12/39) carried homozygous mutations, while 69.2% (27/39) harbored compound heterozygous mutations (Supplementary Table 1). Among the homozygous patients, 66.7% (8/12) harbored the p.V572L mutation. Among the compound heterozygous patients, 25.9% (7/27) exhibited the p.D176V/p.V572L genotype, while the other patients each had a different mutation. With respect to the location of the mutation (i.e., protein domain), 28.2% (11/39) homozygous patients carried mutations only in ED (ED/ED), 46.2% patients (18/39) were compound heterozygotes with 1 mutation each in the ED and KD (ED/KD), and 25.6% patients (10/39) had a mutation in the KD of both genes (KD/KD) (Table 2). The allelic frequencies of p.V572L, p.D165V, p.C13S, and p.R129Q were 35.9% (28/78), 28.2% (22/78), 11.5% (9/78), and 2.6% (2/78), respectively, while all other mutations had only 1 allele each (Supplementary Table 1).

3.3. Respiratory function

None of the patients had lung and/or thoracic diseases that could affect their respiratory function in chest X-ray and/or chest computed tomography. The %VC and %FVC in patients with GNE myopathy were 91.9 (26.9) (range, 18.2–126.3; median, 100.3) and 92.0 (25.8) (range, 16.4–128.5; median, 100.5; Table 1), respectively.

3.4. Patients with respiratory dysfunction

In 30.7% of patients (12/39), %FVC was <80. Of these 12 patients, 91.6% (11/12) were wheelchair-dependent and 83.3% (10/12) had already lost ambulation. Their onset was significantly earlier (19.3 [4.4] vs. 30.3 [8.4], $p < 0.001$) and mean CK level was significantly lower (55.8 [71.6] vs. 279.0 [184.7], $p = 0.004$) than those of patients with normal respiratory function. Four patients exhibited advanced respiratory dysfunction (%FVC < 50% and cough peak flow [CPF] < 160 L/min) (Table 2). All 4 patients had experienced recurrent pneumonia, and 2 patients required nocturnal NPPV. They were all early onset (before 20 years old) and non-ambu-

Table 1
Patient characteristics by respiratory function.

	Total	%FVC ⩾ 80%	%FVC < 80%	
n	*39*	27	12	*p*
Age (years)	43.0 ± 11.3	44.3 ± 11.7	39.9 ± 10.3	0.267
Age at onset (years)	26.8 ± 9.0	30.2 ± 8.4	19.2 ± 4.4	<0.001
GNE/GNE	10 (25.6%)	7 (70.0%)	3 (30.0%)	0.640
GNE/MNK	18 (46.2%)	16 (88.9%)	2 (11.1%)	0.018
MNK/MNK	11 (28.2%)	4 (36.4%)	7 (63.6%)	0.009
Duration from onset of disease to present	16.2 ± 8.4	14.1 ± 7.8	20.8 ± 8.2	0.021
Wheelchair use (%)	27 (69.2%)	16 (59.3%)	11 (40.7%)	0.141
Wheelchair use since (years)	33.3 ± 10.8	37.9 ± 11.3	26.6 ± 5.1	0.002
Lost ambulation	19 (48.7%)	8 (42.1%)	11 (57.9%)	0.014
Age at lost ambulation (years)	36.9 ± 11.9	41.2 ± 11.7	28.2 ± 6.4	0.018
CK (IU/L)	201.3 ± 187.5	279.0 ± 184.7	55.8 ± 71.6	0.004
BMI	21.1 ± 4.2	20.8 ± 3.2	21.9 ± 5.8	0.457
FVC (%)	91.9 ± 26.9	106.9 ± 12.5	58.2 ± 18.7	<0.001
VC (%)	92.0 ± 25.8	106.4 ± 11.6	59.5 ± 17.6	<0.001
CPF (L/min)	334.2 ± 139.5	378.0 ± 105.7	250.2 ± 161.5	0.008

Most patients with reduced respiratory function had already lost ambulation and were entirely wheelchair-dependent. Their onset was significantly earlier and CK levels significantly lower than those of patients with normal respiratory function. FVC: forced vital capacity, VC: vital capacity, CPF: cough peak flow, BMI: body mass index, CK: creatine kinase.

Table 2
Patients with FVC < 50% and CPF < 160 L/min.

Case	Age	Sex	Mutation	Mutant domain	Ambulation status	Disease onset	Disease duration	Age at lost ambulation	%VC	%FVC	CPF (L/min)	Reccurent pneumonea	NPPV	CK (IU/L)	BMI
1	51	Man	p.C13S homozygote	ED/ED	Non-ambulant	17	34	25	18.2	16.4	48.0	Yes	Nocturnal	13	18.6
2	42	Woman	p.V572L homozygote	KD/KD	Non-ambulant	16	26	23	37.6	34.4	141.6	Yes	Nocturnal	13	22.2
3	45	Woman	p.V572L homozygote	KD/KD	Non-ambulant	17	28	31	49.0	48.3	147.6	Yes	No	8	31.6
4	37	Woman	p.V572L homozygote	KD/KD	Non-ambulant	16	21	24	53.7	48.6	118.8	Yes	No	No data	20.4

Table 3
Multivariate regression analysis of predictive factors for respiratory dysfunction.

	Regression coefficient	*p*	Lower limit of 95% confidence interval	Upper limit of 95% CI
Age at onset	0.949	0.042	0.038	1.86
CK	0.068	0.008	0.02	0.115
BMI	−1.8	0.09	−3.811	0.302

Multivariate linear regression analysis was performed to evaluate the relationship between %FVC and other clinical parameters. Age at onset and CK were significantly correlated with %FVC.

lant. The majority (7/12) of patients had KD/KD mutations, whereas significantly fewer patients with respiratory dysfunction had ED/KD mutations.

In order to identify predictive factors for respiratory dysfunction in GNE myopathy, we performed multivariate analysis to determine the relationship with %FVC. This revealed age at onset ($p = 0.042$) and CK ($p = 0.008$) as significantly correlated to %FVC (Table 3, Fig. 1).

Past (5–7 years ago) data were available for 9 patients. The %FVC decrements in 5 patients with respiratory dysfunction were significantly greater than those of patients without dysfunction (20.9 [6.0] vs. 0.8 [9.7], $p = 0.004$; Supplementary Table 2).

4. Discussion

To our knowledge, we are the first to report respiratory dysfunction in GNE myopathy. Our study demonstrates that (1) certain GNE myopathy patients in Japan exhibit respiratory dysfunction, and (2) early onset and lower CK levels resulting from severe muscle atrophy and weakness, and KD/KD mutations can be risk factors for respiratory dysfunction.

Malicdan et al. reported that pathological changes in the diaphragms of the GNE (−/−) hGNED176V-Tg model mice were variable and ranged from almost normal to the presence of marked fibrosis and rimmed vacuoles. On the other hand, the gastrocnemius muscles of all mice exhibited myopathic features [5]. The features in these mice correspond to individual differences observed in the patients of our study. The fact that not all cases in our study exhibited respiratory dysfunction as observed in the GNE (−/−)

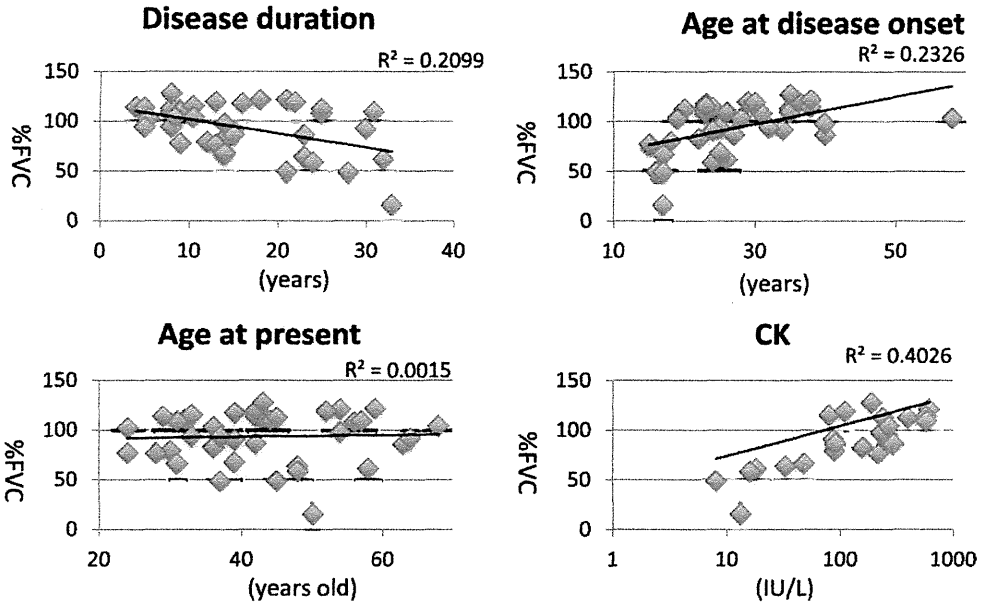

Fig. 1. Scatterplots of %FVC as functions of age, age at disease onset, disease duration, and creatine kinase (CK) level. Age at disease onset, disease duration, and CK level were correlated with %FVC.

hGNED176V-Tg mice indicates that severe respiratory muscle involvement is not a constant feature of GNE myopathy. Yet, since about 30% of patients had decreased %FVC and severe respiratory dysfunction was overlooked by neurologists or physicians, clinicians should be made more aware of the possibility of respiratory dysfunction, particularly in patients with advanced GNE myopathy. If %VC decreases to 70%, patients should be taught air stacking as with other neuromuscular disorders [4,6]. CPF should be routinely measured in patients with GNE myopathy, given that its decrement was associated with recurrent pneumonia in our study. Early induction of assisted CPF and/or MI-E is required if patients with reduced CPF have an airway infection. Serial data suggest that %FVC decreased from the normal range to %FVC < 80, indicating that continuous monitoring is required even in patients with normal respiratory function. Moreover, respiratory function parameters may provide quantitatively useful data for clinical trials, particularly those directed to non-ambulant patients.

All 4 patients with severe respiratory dysfunction exhibited early onset, homozygous mutations, and advanced muscle weakness. However, not all early onset, homozygous, or non-ambulant patients exhibited severe respiratory dysfunction. Although the underlying reasons are unclear, we also found that ED/KD mutations were less associated with decreased respiratory function, while many patients with KD/KD mutations showed respiratory dysfunction. A large scale, cross-sectional study could better identify key factors responsible for respiratory dysfunction and genotype-phenotype correlations.

We are aware that the recruitment of patients from NCNP, highly specialized for muscle disease, is a potential source of selection bias, because they may be particularly more severely affected than the general patient population. Therefore, our study may not correctly reflect the general patient population. Investigations of small populations may underestimate the statistical significance as well. However, our previous GNE myopathy questionnaire study revealed a similar correlation between genotypes and phenotypes [7]. We are currently in the process of establishing a Japanese national GNE myopathy patient registry called Registration of Muscular Dystrophy (REMUDY, http://www.remudy.jp) to perform a broader epidemic investigation of associated conditions, including respiratory dysfunction. To clarify the relationship between respiratory dysfunction and other clinical/laboratory factors, we have initiated a prospective observational study on GNE myopathy.

Three of 4 patients with severe respiratory dysfunction had homozygous p.V572L mutations. Given the frequency of the p.V572L mutation in the Japanese population, it will be interesting to determine whether non-Japanese individuals harboring this mutation also exhibit respiratory dysfunction.

In conclusion, advanced GNE myopathy patients are at risk for respiratory dysfunction. The KD/KD genotype, early onset, loss of ambulation/wheelchair use, and low CK level resulted in advanced muscle atrophy may be associated with respiratory dysfunction.

Acknowledgments

We thank members of the Patients Association for Distal Myopathies in Japan (PADM). This work was partly supported by Research on Intractable Diseases of Health

and Labour Sciences Research Grants, Comprehensive Research on Disability Health and Welfare Grants, Health and Labour Science Research Grants, Intramural Research Grant (23-5/23-4) for Neurological and Psychiatric Disorders from the NCNP, and Young Investigator Fellowship from the Translational Medical Center, National Center of Neurology and Psychiatry.

Appendix A. Supplementary data

Supplementary data associated with this article can be found, in the online version, at http://dx.doi.org/10.1016/j.nmd.2012.09.007.

References

[1] Nonaka I, Sunohara N, Satoyoshi E, Terasawa K, Yonemoto K. Autosomal recessive distal muscular dystrophy: a comparative study with distal myopathy with rimmed vacuole formation. Ann Neurol 1985;17:51–9.

[2] Argov Z, Yarom R. "Rimmed vacuole myopathy" sparing the quadriceps. A unique disorder in Iranian Jews. J Neurol Sci 1984;64:33–43.

[3] Udd B, Griggs RC. Nonaka myopathy. In: Engel AG, Franzini-Armstrong C, editors. Myology. New York: McGraw-Hill; 2004. p. 1178–9.

[4] Bach JR. Noninvasive respiratory muscle aids. In: Bach JR, editor. Management of patients with neuromuscular disorders. Philadelphia: Hanley & Belfus; 2004. p. 211–69.

[5] Malicdan MC, Noguchi S, Nonaka I, Hayashi YK, Nishino I. A Gne knockout mouse expressing human GNE D176V mutation develops features similar to distal myopathy with rimmed vacuoles or hereditary inclusion body myopathy. Hum Mol Genet 2007;16:2669–82.

[6] Bach JR. Pulmonary defense mechanisms and cough peak flow. In: Bach JR, editor. Management of patients with neuromuscular disorders. Philadelphia: Hanley & Belfus; 2004. p. 193–9.

[7] Mori-Yoshimura M, Monma K, Suzuki N, et al. GNE myopathy (distal myopathy with rimmed vacuoles) patients with mutations in the UDP-GlcNAc 2-epimerase and in the *N*-acetylmannosamine kinase domains of the GNE gene exhibit less severe phenotypes than patients with mutations only in MNK domain. J Neurol Sci, 2012. [Epub ahead of print].

Acta Neuropathol
DOI 10.1007/s00401-012-1073-6

ORIGINAL PAPER

VMA21 deficiency prevents vacuolar ATPase assembly and causes autophagic vacuolar myopathy

Nivetha Ramachandran · Iulia Munteanu · Peixiang Wang · Alessandra Ruggieri · Jennifer J. Rilstone · Nyrie Israelian · Taline Naranian · Paul Paroutis · Ray Guo · Zhi-Ping Ren · Ichizo Nishino · Brigitte Chabrol · Jean-Francois Pellissier · Carlo Minetti · Bjarne Udd · Michel Fardeau · Chetankumar S. Tailor · Don J. Mahuran · John T. Kissel · Hannu Kalimo · Nicolas Levy · Morris F. Manolson · Cameron A. Ackerley · Berge A. Minassian

Received: 11 July 2012 / Revised: 20 November 2012 / Accepted: 5 December 2012

Abstract X-linked Myopathy with Excessive Autophagy (XMEA) is a childhood onset disease characterized by progressive vacuolation and atrophy of skeletal muscle. We show that XMEA is caused by hypomorphic alleles of the *VMA21* gene, that VMA21 is the diverged human ortholog of the yeast Vma21p protein, and that like Vma21p, VMA21 is an essential assembly chaperone of the vacuolar ATPase (V-ATPase), the principal mammalian proton pump complex. Decreased VMA21 raises lysosomal pH which reduces lysosomal degradative ability and blocks autophagy. This reduces cellular free amino acids which leads to downregulation of the mTORC1 pathway, and consequent increased macroautophagy resulting in proliferation of large and ineffective autolysosomes that engulf sections of cytoplasm, merge, and vacuolate the cell. Our results uncover a novel mechanism of disease, namely macroautophagic overcompensation leading to cell vacuolation and tissue atrophy.

Keywords Vacuolar myopathy · Autophagy · Vacuolar ATP-ase · Splicing mutations · Lysosomal acidification

N. Ramachandran and I. Munteanu are both first-authors of this paper.

Electronic supplementary material The online version of this article (doi:10.1007/s00401-012-1073-6) contains supplementary material, which is available to authorized users.

N. Ramachandran · I. Munteanu · P. Wang · A. Ruggieri · J. J. Rilstone · N. Israelian · T. Naranian · R. Guo · Z.-P. Ren · D. J. Mahuran · B. A. Minassian
Program in Genetics and Genome Biology, The Hospital for Sick Children, Toronto, ON M5G 1X8, Canada

I. Munteanu · J. J. Rilstone · B. A. Minassian
Institute of Medical Sciences, University of Toronto, Toronto, ON M5S 1A8, Canada

Present Address:
I. Munteanu
Dubowitz Neuromuscular Centre, UCL Institute of Child Health, London WC1N 1EH, UK

P. Paroutis · C. S. Tailor
Program in Cell Biology, The Hospital for Sick Children, Toronto, ON M5G 1X8, Canada

I. Nishino
Department of Neuromuscular Research, National Center of Neurology and Psychiatry, Kodaira, Tokyo 187-8502, Japan

B. Chabrol
Unité de Médecine Infantile, Hôpital D'enfants, CHU de la Timone, 13385 Marseille, France

J.-F. Pellissier
Laboratoire d'Anatomie Pathologique et Neuropathologie, Hôpital de la Timone, 13385 Marseille, France

C. Minetti
Muscular and Neurodegenerative Disease Unit, G. Gaslini Institute and University of Genova, 16147 Genoa, Italy

B. Udd
Department of Neurology, Vaasa Central Hospital and Tampere University, FI-65130 Vaasa, Finland

M. Fardeau
Myology Institute, Salpetriere Hospital, 75013 Paris, France

J. T. Kissel
Department of Neurology, Ohio State University, Columbus, OH 43210, USA

Published online: 12 January 2013

Introduction

Vacuolar ATPases (V-ATPases) are ubiquitous in endomembrane systems of all eukaryotic cells. They are vital proton pumps that acidify lysosomes and regulate the pH of multiple cell processes, including the secretory endovesicular systems which use gradated pH to accomplish stepwise modifications. The V-ATPase is composed of 14 subunits organized into a transmembrane (V_0) and a cytoplasmic (V_1) sector, and has a unique rotary pumping mechanism (Supplemental Fig. 1) [8]. In yeast, V_0 assembly occurs in the endoplasmic reticulum (ER), coordinated by the Vma21p chaperone [18]. V-ATPase subunits are highly conserved from yeast to man, but the closest mammalian sequence to yeast Vma21p has <22 % similarity and lacks a critical dilysine signal [18] making it unclear whether this predicted protein (LOC203547) is indeed the Vma21p ortholog. To date, all disease-causing mutations in V-ATPase subunits are in specialized subunit isoforms that confer specialized functions [8]. For example, mutations in the a3 isoform of subunit 'a' cause osteopetrosis [9]. This isoform is osteoclast-specific and targets the V-ATPase to the osteoclast plasma membrane to acidify its extracellular space to resorb bone. Diseases with mutations in the ubiquitous subunits common to all V-ATPases have not been reported [8].

X-linked myopathy with excessive autophagy (XMEA, OMIM 310440) [12] is a skeletal muscle disorder affecting boys and sparing carrier females. Onset is in childhood with weakness of the proximal muscles of the lower extremities, progressing slowly to involve other muscle groups, and toward loss of independent ambulation after age 50. Other organs, including heart and brain, are clinically unaffected. Pathological analysis of skeletal muscle shows no inflammation, necrosis or apoptosis (Supplemental Figs. 2, 3). Instead, myofiber demise occurs through a novel form of autophagic cell death characterized by giant autophagic vacuoles 2–10 μm in size encircling sections of cytoplasm including organelles. These vacuoles contain lysosomal hydrolases, yet are unable to complete digestion of their contents. Instead, they migrate to the myofiber surface, fuse with the sarcolemma, and extrude their contents extracellularly forming a field of cell debris around the fiber (Supplemental Fig. 2) [12, 36].

We show that LOC203547 is the human ortholog of Vma21p, and that hypomorphic mutations of the *VMA21* gene disrupt autophagy and cause XMEA. XMEA presents an unusual mechanism of disease where a major housekeeping complex (the V-ATPase) essential to numerous functions of all cells is impaired, but only to the extent of clinically affecting the function with highest V-ATPase dependence, autophagy, in a tissue with high reliance on this function [22, 28] i.e., skeletal muscle.

Patients, materials, and methods

Patients

All patients in this study were males with childhood onset progressive weakness and wasting of skeletal muscle. Proximal muscles of the lower extremities were always initially and later predominantly affected. No other organ system was affected clinically. At least one patient from each family underwent a biopsy, and all biopsies showed the pathognomonic features of XMEA as briefly summarized in the introduction. Detailed clinical and pathological descriptions in the proband from each family are provided in Supplemental Patient Information. Representative microscopic slides are shown in Supplemental Fig. 2. The patients belong to 14 families (XMEA1 through XMEA14). Patient fibroblast cell lines used throughout the paper were from probands from families XMEA 12 and 13, which in the figures, for space considerations, are abbreviated as P1, P2, respectively. Lymphoblasts of probands from families XMEA1, XMEA4, XMEA10, XMEA 12, and 13 were designated as P3, P4, P5, and P6, respectively. Cell lines from normal control individuals are indicated as C.

Mutation identification, RT-PCR, qRT-PCR, and minigene studies

Primer sequences and PCR conditions to amplify LOC203547 exons and flanking sequences for mutation detection are in Supplemental Table 1, which also contains

H. Kalimo
Haartman Institute Department of Pathology, University of Helsinki, FI-00014 Helsingin, Yliopisto, Finland

H. Kalimo
Departments of Pathology and Forensic Medicine, Institute of Biomedicine, University of Turku, FI-20520 Turku, Finland

N. Levy
Faculté de Médecine de Marseille, Inserm UMR_S910, Université de la Méditerranée, 13385 Marseille, France

M. F. Manolson
Faculty of Dentistry, University of Toronto, Toronto, ON M5G 1G6, Canada

C. A. Ackerley
Department of Pathology and Laboratory Medicine, The Hospital for Sick Children, Toronto, ON M5G 1X8, Canada

B. A. Minassian (✉)
Division of Neurology, Department of Paediatrics, The Hospital for Sick Children, Toronto, ON M5G 1X8, Canada
e-mail: berge.minassian@sickkids.ca

all other primer sequences used in this study. For RT-PCR of LOC203547 mRNA in patient lymphoblasts or fibroblasts and of minigene mRNAs following transfection in C2C12 cells, 1 μg total RNA was converted into cDNA using oligo (dT) primers and then PCR-amplified for 20 cycles. For qRT-PCR of these mRNAs, relative standard curves normalized to β-actin were used. The standard curves were prepared from control lymphoblasts or C2C12 cDNA at 1, 10, 10^2, 10^3, and 10^4 dilution factors. Individual reactions contained 0.5 μL template cDNA of appropriate concentration for linear amplification based on the standard curve, 100 ng of each primer, and 1xSYBR Green PCR master mix (Applied Biosystems) to a final volume of 20 μL. Reactions were carried out using Applied Biosystems 7900HT for 40 cycles (95 °C, 15″; 60 °C, 60″). PCR product purity was determined by melting curve analysis. Each cDNA preparation was tested in triplicate. Data were analyzed using SDS2.1 v.2.1.0.3 (Applied Biosystems). Values exceeding two standard deviations were excluded. Construction of the minigenes is described in Supplemental Methods and Supplemental Fig. 5.

V-ATPase assays

Total protein was measured using the Bradford assay and a BSA standard curve. Hydrolysis of ATP by V-ATPase was measured by the bafilomycin A1-sensitive method adapted from Huss et al. [11]. Microsomal pellets were thawed on ice and suspended in ATPase buffer (10 mM HEPES-Tris pH 7, 5 mM MgCl2, 50 mM KCl, 10 mM NaN_3, 1 mM levamisole–10 mM NaF, 0.7 μg/ml leupeptin, 0.7 μg/ml pepstatin A, 48.72 μg/L PMSF) to a protein concentration of 0.75–1.75 mg/ml (see Supplemental methods for subcellular fractionation procedures). The reaction mix contained 1 mM ATP substrate, 3 μg total protein samples, 5 μM valinomycin, 5 μM nigericin, 1 mM orthovanadate, 10 μg/mL oligomycin in ATPase buffer made to 70 μL final volume and incubated in the presence and absence of 10 nM bafilomycin for 30′ at 37 °C. ATP hydrolysis was terminated with 13 % SDS and 100 mM EDTA. Control reactions were done to correct any non-enzymatic hydrolysis of ATP or orthophosphate contamination from reagents by adding the stop solution prior to ATP substrate addition. Reaction was initiated by addition of Taussky-Shorr color reagent (0.5 % w/v $FeSO_4$, 0.5 % w/v ammonium molybdate, and 0.5 M H_2SO_4) [35]. The reaction was incubated for 20′ at RT and inorganic phosphate (P_i) was measured by absorbance at 650 nm. Standard calibration curve was generated using (P_i) standards (0, 2.5, 5, 10, 25, 50, 100, and 150 nmole). Mean values and standard deviation were calculated from three independent assay repeats done in triplicate.

Complementation assay

Saccharomyces cerevisiae BY4742 wild-type strain (MATα, his3Δ1, leu2Δ0, lys2Δ0, and ura3Δ0) and *vma21*Δ mutant (BY4742, Matα, his3Δ1, leu2Δ0, lys2Δ0, ura3Δ0, and YGR105w::kanMX4) were obtained from the European Saccharomyces Cerevisiae Archive for Functional Analysis (Euroscarf). LOC203547 was cloned into yeast expression plasmid pCADNS under alcohol dehydrogenase (*ADH)* promoter, terminator, and transformed into strains BY4742 and *vma21*Δ. Transformants were selected on synthetic complete media without leucine and assayed for viability on medium containing 10 mM $CaCl_2$, YPD pH 7.5 (alkaline conditions), and ability to grow on glycerol as the sole carbon source.

Determination of lysosomal pH

Lysosomal pH was measured according to Demaurex et al. [6]. Fibroblasts were seeded on 25 mm circular glass cover slips and grown to confluence in DMEM with 10 % FBS at 37 °C and 5 % CO_2. At confluence, cells were washed twice with PBS and serum-starved by adding DMEM containing 2 % FBS for 40 min. Lysosomes were loaded overnight with 0.5 mg/ml dextran-coupled Oregon Green 514 (Molecular Probes) in DMEM supplemented with 10 % FBS, chased for 2 h in DMEM (10 % FBS), and washed to remove residual dextran. Ratiometric fluorescence microscopy was performed using a Leica DMIRB microscope with 100X (1.4 NA) oil objective. Fluorescence images were acquired at excitation wavelengths of 440 ± 10 and 490 ± 10 nm. Image acquisition and analysis were performed using software MetaMorph (Universal Imaging). Regions of interest (ROI), representing late endosomes/lysosomes as resolved by light microscopy, were defined as areas above a certain fluorescence threshold in the 490 nm excitation channel. Mean intensity ratio between 490 and 440 nm excitation channels was calculated for each ROI, and mean ratio weighted by ROI size was then calculated for each imaged fibroblast. Calibration curves were obtained after 4 min equilibration in nigericin (5 μm) containing MES buffers (in mM: 30 NaCl, 130 KCl, 30 $MgCl_2$, 25 MES, and 20 glucose) with different pH values adjusted between pH 3.0 and 7.0. Ratios were converted to pH using the calibration curve fitted to a sigmoidal equation. At least six lysosomes within the same cell (at least five cells per sample) were covered, and the experiment was repeated six times for significance.

Long-lived protein degradation

Intracellular protein degradation was measured as described by Cuervo et al. [5]. Confluent cells were labeled with

200 μCi/ml [S]methionine/[S]cysteine Redivue in vitro cell labeling mix for 48 h at 37 °C, and washed and maintained in complete medium with excess of unlabeled methionine and leucine. Following this, aliquots of media and cells were taken at different times for 72 h and precipitated in TCA, and proteolysis was measured. Media contained MG-132 to eliminate proteasomal contribution. Total radioactivity incorporated in cellular proteins was determined in triplicate samples as the amount of acid-precipitable radioactivity. Proteolysis was calculated as the % acid-precipitable radioactivity (protein) transformed into acid-soluble radioactivity (amino acids and peptides) at the different analyzed time points. Values were expressed as % protein degraded. In separate sets, the above proteolysis experiments were performed in the presence of 15 mM NH_4Cl and 100 μM leupeptin or 10 mM 3-methyladenine (3MA) in the culture medium during the chase. The former combination effectively blocks all types of autophagy [27] and 3MA blocks macroautophagy [20]. The inhibitory effect on the lysosomal system was calculated as the decrease in protein degradation sensitive to NH_4Cl/leupeptin. Non-lysosomal proteolysis was subtracted from total proteolysis (the former was negligible, <3 %, and unvarying). The inhibitory effect on macroautophagy was determined as the decrease in protein degradation sensitive to NH_4Cl/leupeptin that is also inhibited by 3MA. Non-macroautophagy-dependent degradation was calculated as the % protein degradation sensitive to NH_4Cl/leupeptin that is not inhibited by 3MA.

Knockdown of VMA21 mRNA

pSUPER RNAi system [3] was used for specific downregulation of mouse *Vma21* expression. RNAi expressing sequences (Supplemental Table 1) for targeting the 3′UTR region of *Vma21* were cloned into pSUPER RNAi system. Forward and reverse strands of the oligonucleotides were annealed to form a duplex and were inserted into *Bgl*II–*Hin*dIII cleavage site of the pSUPER RNAi vector prelinearized with restriction enzymes. The recombinant plasmid was transformed into XLBlue *E.coli* strain, and the resultant cells were cultured in LB-ampicillin containing media. Recombinant clones positive for siRNA were selected and used to transfect NIH3T3 cells. Downregulation of *Vma21* was assessed using quantitative RT-PCR and Western blotting. A mock transfection with empty pSUPER vector was used to control any non-specific effects. The transfected cells were examined for phenotypic changes with electron microscopy.

Amino acid starvation, and stimulation with leucine or leucine ester

Amino acid starvation methods were adapted from Zoncu and colleagues [38]. Control and patient fibroblasts grown in DMEM with 10 % dialysed FCS were rinsed three times with amino acid-free RPMI and incubated in the same for 4 h. After a 4-hour starvation period, cells were stimulated by adding leucine or leucine methyl ester for 20 min (not exceeding a final concentration of 0.05 mM) in RPMI in independent experiments. The cells were lysed using RIPA buffer with protease inhibitor cocktail, and Western blot was performed using anti-phospho p70S6 kinase antibody.

Measurement of total amino acids

The samples for estimation of free amino acid concentration were prepared based on a previously described method [10]. Fibroblasts grown to confluence in DMEM with 10 % FBS were scraped and frozen in 200 μl of phosphate buffered saline at −80 °C for 15 min and thawed at 4 °C followed by 20 °C for one cycle. For the next cycle of freeze–thaw, samples were kept at 4 °C for an hour followed by 6–8 min at 20 °C. For the third freeze thaw cycle, cells were frozen again at −80 °C for 15 min, and thawed 40 min at 4 °C and 8 min at 20 °C. The third cycle was repeated three times. The free amino acid concentration was determined by a colorimetric method ($\lambda = 570$ nm) using the amino acid quantitative kit from Biovision as per the manufacturer's instructions. To generate a standard curve, 0, 2, 4, 6, 8, and 10 μl of L-amino acid standard was added to each well to generate 0, 8, 16, 24, 32, and 40 nmol/well concentration. The final volume was adjusted to 100 μl/well using L-amino acid assay buffer. The reaction mix consisted of 46 μl of amino acid assay buffer, 2 μl amino acid probe, and 2 μl L-amino acid enzyme mix. To measure the concentration in test samples, the standards and the samples were incubated in 50 μl of reaction mix in a total volume of 150 μl made up with the assay buffer and incubated for 30 min at 37 °C. L-amino acid amount (nmol) was calculated from the standard curve based on absorbance at OD 570 and expressed as nmol/number of cells in each well. Additional controls including a protein BSA sample, a mixture of pure amino acids, and a mixture of protein with amino acids were used to check for false positive results.

Mass spectrometric analyses of intracellular leucine

The intracellular leucine concentrations in patient and control fibroblasts were quantified using LC–MS-MS, applying a modification of a previously described method [30]. Fibroblasts grown to confluence were scraped and centrifuged at 3000 rpm for 10 min at 4 °C. Cell pellets were resuspended in 500 μl methanol and subjected to sonication. 75 μl of cell homogenate was transferred into eppendorf tubes, internal standard (L-leucine-d10 5 ng) added and made up to 1 ml with methanol for protein

precipitation. The mixture was vortexed and centrifuged at 15,000×*g* for 15 min at 4 °C. Supernatants were transferred to new screw cap tubes and dried under nitrogen gas. Dried residues were derivatized with 100 µl 3 M HCl-butanol at 65 °C for 20 min. The dried butylated samples were reconstituted in 1 ml of 20 % acetonitrile and 0.1 % formic acid, and transferred to a set of borosilicate autosampler vials for injection. Both samples and standard curve were analyzed by liquid chromatography-mass spectrometry MS/MS in a API 4000 triple quadrupole mass spectrometry system (Applied Biosystems). Prior to entering the triple quadrupole MS, leucine was separated from isoleucine using a Dionex Acclaim (Thermo Scientific) organic acid column (5 µm 120 A, 4.0 × 250 mm; Dionex), and was eluted over 6 min at a flow rate of 450 µl/min with an Agilent HPLC 1200. The following butylated transitions were employed: for leucine m/z 188.10/86.100 and for leucine-d10 m/z 198.200/86.100. The concentration of L-leucine was measured by running against L-leucine standard curve (0.5–500 ng) spiked with the same amount of internal standard (L-eucine-d10 5 ng). Endogenous leucine concentrations were calculated using the slope and the positive y-intercept of the calibrators by the Analyst 1.5.2 software (Applied Biosystems/MDS SCIEX). The expected ratio of leucine to the IS (leucine-d10) was plotted against the observed peak area ratio of the analyte to IS to extract the slope and intercept.

Statistical analysis

All statistical analysis was performed by 2-tailed Student's *t* test using Microsoft Excel. A P value <0.05 were considered significant. Data are expressed as mean ± SEM or as mean ± SD as indicated in corresponding legends. All Western blots were repeated three times to validate the results. Where protein levels were compared, the band intensities measured using Image J program are specified in the corresponding figure legends.

Results

Hypomorphic mutations in the LOC203547 gene cause XMEA

We previously mapped the XMEA gene to a 0.58 Mb region of Xq28 containing four known genes and a predicted fifth gene, LOC203547 [23] (Fig. 1a). We sequenced the exons and flanking intronic sequences of all five genes in XMEA patients from 14 families, and found sequence changes only in LOC203547 which in all families segregated with the disease. To confirm that the changes are mutations, we sequenced LOC203547 in over 450 control chromosomes, including 100 from ethnically matched individuals for each mutation, none of which contained the identified changes (Fig. 1b).

LOC203547 has three exons, and a 4.7 Kb transcript expressed ubiquitously (Supplemental Fig. 4a). The mutations consist of six different single-nucleotide substitutions. The first two, c.54–27A>T and c.54–27A>C, eliminate the A nucleotide defining the splice branch point of intron 1. The third, c.163+4A>G, removes the A in the +4 position after exon 2, which contributes to optimal U1 snRNA binding during splicing. The fourth, c.164–7T>G, disrupts the polypyrimidine tract in intron 2, which would reduce the binding efficiency of the U2AF splice factor. The fifth, c.272G>C, is in coding sequence replacing a glycine with alanine, but also abolishes a predicted splice enhancer site. The sixth, c.*6A>G, occurs six nucleotides past the termination codon in the 3′UTR (Fig. 1).

Splice site mutations cause disease by generating abnormal isoforms, or by decreasing mRNA quantity through reduced splicing efficiency. We detected no splice variants by RT-PCR or by Northern blotting (Supplemental Fig. 4B), but a comparison of means of RNA levels by quantitative RT-PCR (qRT-PCR) from patient fibroblasts and lymphoblasts revealed 32–58 % reduction in LOC203547 mRNA, including in patients with the 3′UTR mutation (Fig. 2a, b). Western blots and immunocytochemistry showed that LOC203547 is also reduced at the protein level (Fig. 2c, d). To confirm that these reductions are directly caused by the LOC203547 variants and not secondary disease effects, we generated minigene expression vectors for each splice site change (Supplemental Methods and Supplemental Fig. 5) and transfected them into C2C12 myoblasts. In these experiments, the only difference between each minigene and corresponding wild-type minigene are the single altered LOC203547 nucleotides observed in the patients. qRT-PCR showed >40 % decrease in mRNA from the variant minigenes compared to wild-type (Fig. 2e, f), confirming that the changes cause LOC203547 mRNA downregulation.

LOC203547 is the human ortholog of the yeast V-ATPase assembly chaperone Vma21p

Toward determining whether LOC203547 is the human ortholog of Vma21p we first asked whether its downregulation in XMEA affects the V-ATPase and whether this effect is comparable to the previously characterized effect of Vma21p deficiency in yeast. The yeast *vma21* deletion mutant *vma21*Δ has markedly reduced V-ATPase levels and V-ATPase activity and defective growth. It also exhibits increased free V_1 sector proteins in the cytosol, because V_1 subunits are produced in the cytosol and subsequently added to the V_0 sector assembled in the ER [18].

a

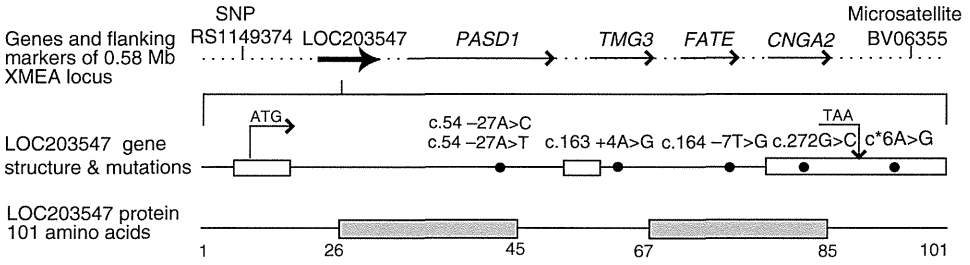

b

Family, ethnicity and number of affected patients per family			Mutation	Relevance, predicted outcome	Controls* T	Controls* E
XMEA-1	American	3	c.54 –27A>C	The mutated A nucleotide is the predicted splicing branch point**. The mutation would inhibit nucleophilic attack of the branch point onto the 5' splice site of the first intron during splicing.	360	133
XMEA-2	Italian	1			360	108
XMEA-3	French	1	c.54 –27A>T		360	119
XMEA-4	French	2	c.163 +4A>G	The fourth position after an exon is A in 70% of all exons. This mutation is expected to result in suboptimal binding of the U1 snRNA to the 5' splice site.	360	119
XMEA-5	French	2			360	119
XMEA-6	French	2			360	119
XMEA-7	French	4	c.164 –7T>G	This mutation introduces a purine into the polypyrimidine tract of this splice site. This is predicted to decrease the binding strength of the U2AF splice factor.	465	122
XMEA-8	French	2			465	122
XMEA-9	French	5			465	122
XMEA-10	Finnish	5	c.272G>C	This coding mutation is predicted to disrupt a binding motif for the SC35 splice factor***. It also changes a glycine to alanine.	304	84
XMEA-11	Finnish	2			304	84
XMEA-12	Armenian	7	c.*6A>G	3' UTR mutation in proximity to the stop codon. This mutation may disrupt binding of transcript stabilization and processing factors.	304	92
XMEA-13	American	10			304	128
XMEA-14	American	3			304	128

Fig. 1 LOC203547 and XMEA mutations. **a** The LOC203547 gene has three exons (*open boxes*). The positions of the six XMEA mutations relative to the LOC203547 exons are depicted by *bullets*. The LOC203547 protein has two predicted transmembrane domains (*grey boxes*). **b** Table of mutations. In the electropherogram panels, *top* is normal sequence and *bottom* sequence is the patient's. * numbers of chromosomes from normal individuals genotyped for each mutation, T is the total number of chromosomes, E is the number of chromosomes from ethnically matched individuals; ** Prediction by Splicing Sequences Finder—Branch Point Sequence (http://www.umd.be:2300/searchBP.html); *** Prediction by Exonic Splicing Enhancer Finder (http://rulai.cshl.edu/cgi-bin/tools/ESE3/esefinder.cgi?process=home)

We measured V-ATPase activity in the light membrane fraction (includes all organelles) of XMEA patient lymphoblast extracts and found that it is reduced to 12–22 % of normal (Fig. 3a). In fibroblasts, V-ATPase activity was reduced to 11–13 % of normal, and in fresh-frozen muscle biopsies to 21–33 % (Fig. 3b). We next assessed the amount of V-ATPases in the light membrane fractions by performing immunoprecipitation and Western blot

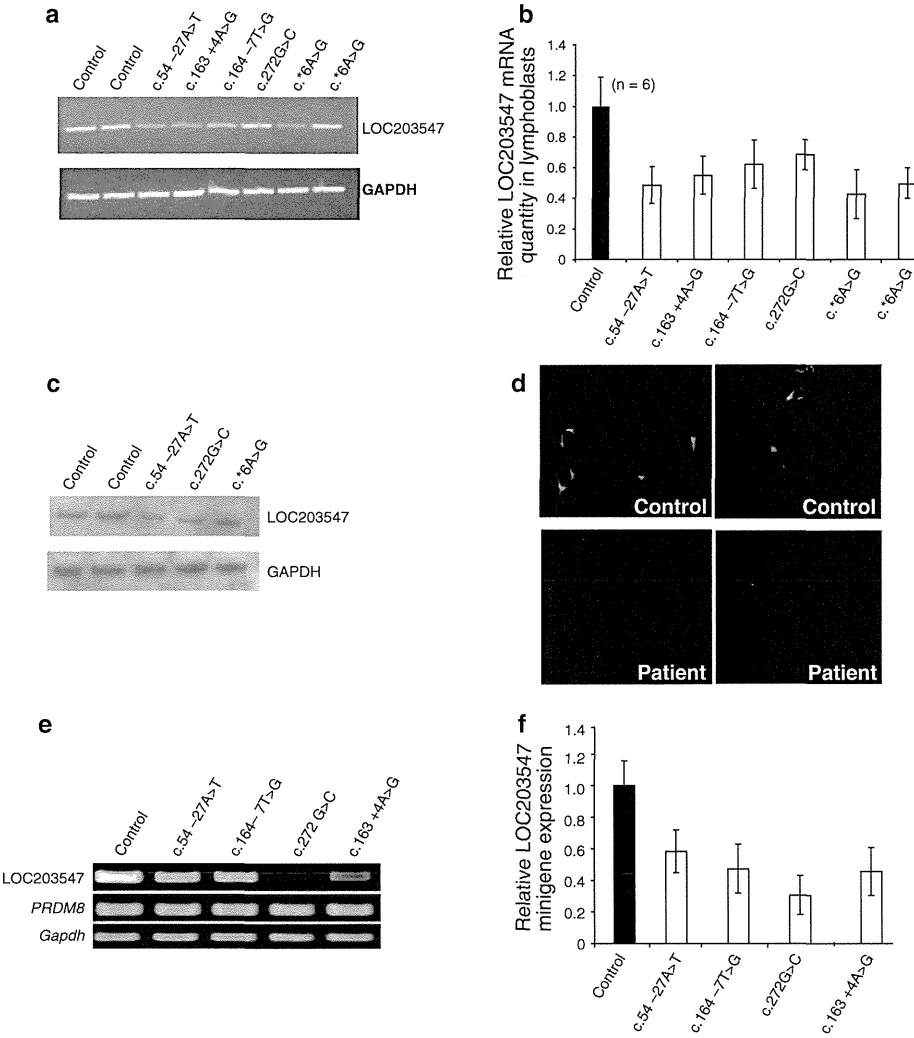

Fig. 2 Effects of XMEA mutations on LOC203547 mRNA and protein. **a** RT-PCR of LOC203547 from patient and control lymphoblast RNA. **b** Quantitative RT-PCR of LOC203547 in lymphoblast RNA measured as a ratio to β-actin. **c** LOC203547 protein in frozen patient and control skeletal muscle by Western blot; mean band intensities were measured using Image J: Control ($n = 2$) 1.19 ± 0.074; patient ($n = 3$) 0.46 ± 0.045. Similar results in fibroblasts shown in Supplemental Fig. 4c. **d** LOC203547 protein in patient (XMEA-13) and control fibroblasts by immunofluorescence light microscopy. **e** RT-PCR of four LOC203547 minigene constructs following transfection into C2C12 myoblasts, the *PRDM8* gene (in pcDNA 3.1) was cotransfected as transfection efficiency control, endogenous *GAPDH* expression was used as control for cDNA synthesis. **f** Quantitative RT-PCR of above minigenes relative to β-actin. *Bars* in panels **b** and **f** represent mean ± standard deviation of three independent experiments

experiments with antibodies against the V-ATPase subunits a and E which showed reduced signal in patients (Fig. 3c, d) indicating that the decreased V-ATPase activity was due to decreased V-ATPase levels which we confirmed by directly counting V-ATPase complexes on intact membranes of intact neutrophils using immunogold electron microscopy (Fig. 3e, f). Western blots of cytosolic and light membrane fractions showed that V_1 subunit E was increased in patient cytosols to an extent similar to its reduction from organellar membranes (Fig. 3d), indicating that the decrease in V-ATPases is due to decreased formation of V_0 complexes. As an assembly chaperone, yeast Vma21p expectedly interacts with the V_0 complex, and immunoprecipitating it co-precipitates the complex [18]. We show that immunoprecipitating LOC203547 in light membrane fractions of mammalian cells likewise co-precipitates V_0 (Fig. 4a, b), and immunocytochemical experiments show co-localization of LOC203547 with V-ATPase subunits (Supplemental Fig. 6). The contact between yeast Vma21p and V_0 is the V_0 subunit c' [18]. Subunits c' as well as c and c" are highly homologous proteins that form the yeast V_0 intramembranous rotating cylinder (Supplemental Fig. 1). c' does not exist in mammalian proteomes, and in mammals the V_0 rotating core

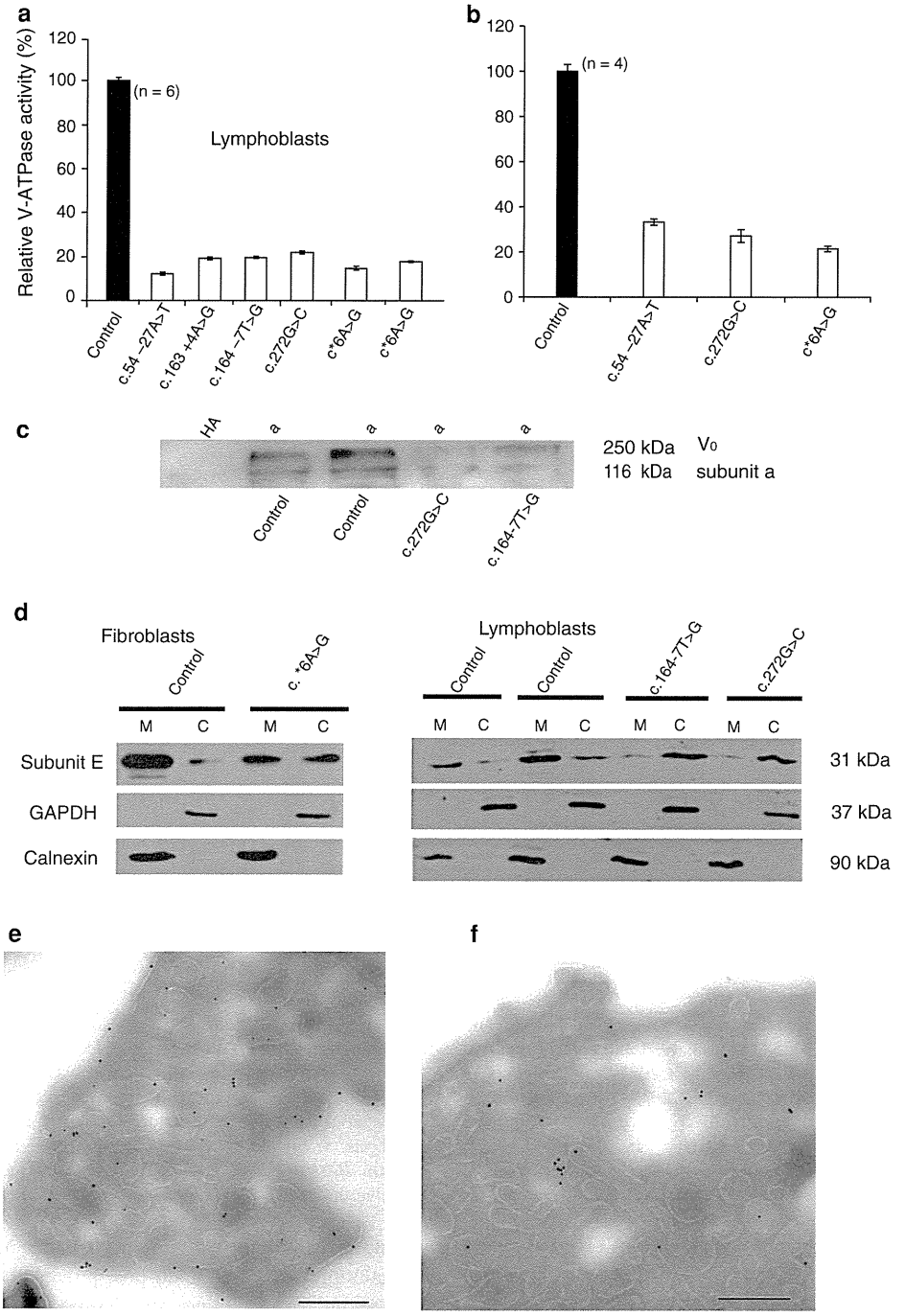

utilizes only proteins c and c" [8]. We, therefore, tested whether LOC203547 interacts with either of these proteins. Immunoprecipitating LOC203547 following full denaturation revealed that subunit c", but not subunit c, remained bound (Fig. 4c), suggesting that LOC203547 interfaces with the V_0 complex at least in part through c".

Finally, we asked whether LOC203547 can complement *vma21*Δ. The *vma21*Δ yeast strain is characterized by a well-defined set of growth defects including poor growth on complete media, and the absence of growth on media with nonfermentable carbon sources or with high pH or calcium [18]. We cultured *vma21*Δ, LOC203547-transformed

◀**Fig. 3** Defective V-ATPase activity and assembly in XMEA. **a**, **b** V-ATPase activity in lymphoblast and skeletal muscle light membrane fractions; *bars* mean ± standard error of three independent experiments. **c** Immunoprecipitation and Western blotting of lymphoblast light membrane fractions with subunit a antibody, non-denaturing conditions (DTSSP crosslinking and detergent C12E9) used to favor maintaining V_0 assembled. V_0, which includes subunit a, is 250 kDa in size; subunit a is 116 kDa. In patients, both are reduced (subunit a is known to undergo rapid degradation when unassembled) (2). **d** Western blots of V_1 subunit E in light membrane (Mem) and cytosolic (Cyt) fractions. E is decreased from light membrane fractions and increased in cytosol; band intensities in patients determined using image J software: in fibroblasts from patient c.6*A>G, 0.509 (Mem) and 0.711 (Cyt) vs 1.293 (Mem) and 0.298 (Cyt) in control; in lymphoblasts from patient c.164-7T>G, 0.120 (Mem) and 0.743 (Cyt), and patient c.272G>C, 0.213 (Mem) and 1.251 (Cyt) compared to averages of 0.753 (Mem) and 0.208 (Cyt) in controls. GAPDH and Calnexin used to verify fraction purity. **e**, **f** Representative EM of neutrophils from normal (**e**) and XMEA (**f**) cells immunogold labeled against subunit a; neutrophils possess large V-ATPase-rich phagosomes, and V-ATPases in the plasma membrane utilized for migration through tissues. In XMEA, gold particle numbers are reduced (*black dots* at the plasma membrane and on the membranes of the phagosomes); *bar*, 0.5 μm. Actual mean counts from 150 neutrophils from three controls (50 cells per control) and 100 neutrophils from two patients (50 cells/patient) were, in particles/linear μm: control plasma membrane, 2.7 ± 0.5, patient plasma membrane, 0.4 ± 0.1; control phagosome membrane, 4.3 ± 0.75, patient phagosome membrane, 1.25 ± 0.06; significance <0.001 (student's *t* test)

*vma21*Δ, and wild-type yeast for 3 days in YP-glycerol pH 5.5 (glycerol as sole carbon source), YPD pH 7.5 (elevated pH), or YPD pH 5.5 with 10 mM $CaCl_2$. *Vma21*Δ showed characteristic negligible growth, while LOC203547-transformed *vma21*Δ grew proficiently, and equal to wild-type, on all three media (Fig. 4d), showing that LOC203547 fully rescues *vma21*Δ. Collectively, these results establish that LOC203547 is the human ortholog of Vma21p, and is, hereafter, named VMA21.

The subcellular stations of VMA21 diverge from those of Vma21p

In yeast, Vma21p first interacts in the ER membrane with the V_0 subunit c'. This initiates a stepwise assembly of the other V_0 components, and the presence of Vma21p is necessary throughout the process. Once V_0 is formed, Vma21p accompanies it on COPII vesicles to the Golgi apparatus, where V_1 subunits are added to complete the V-ATPase [18]. Vma21p is retargeted by its carboxy-terminal dilysine signal to the ER, while each V-ATPase is directed to its particular destination based on which isoform of the 'a' subunit was incorporated during V_0 assembly [18]. To determine the subcellular locations in which human VMA21 acts, we stained human fibroblasts (Fig. 5) and C2C12 cells (Supplemental Fig. 7) with VMA21 and organelle-specific antibodies. VMA21 strongly localizes at ER, COPII vesicles, and the ER-Golgi intermediate compartment (ERGIC). It is not present at the Golgi, or beyond (trans-golgi network). VMA21 lacks a dilysine ER return signal consistent with which we find that it has minimal, if any, presence on COPI, the ER return vesicle. There was also no localization on mitochondria and minimal, likely negligible, signal in few peroxisomes and lysosomes (Fig. 5). In summary, the route of VMA21 is diverged from that of its yeast counterpart. It follows the latter's path from ER to ERGIC, but not on to the Golgi, and it does not appear to cycle back to the ER.

Block in the completion of autophagy, associated with upregulation of its initial phases

Autophagy is the degradation of long-lived proteins and other cell components. It is composed of three processes with a common final stage, digestion at low pH by lysosomal hydrolases. In chaperone-mediated autophagy, proteins are taken into lysosomes via receptors. In microautophagy, they are engulfed by lysosomes. In macroautophagy, isolation membranes form in the cytoplasm, surround targeted proteins and other constituents, and fuse with lysosomes. The transitional structures prior to merger with lysosomes are called autophagosomes, and the final organelles autolysosomes. Macroautophagy is the largest contributor to autophagy, and is the process that expands to compensate for insufficiencies in the non-macro autophagic processes, or to meet increased autophagic demands such as during starvation [21].

Based on our finding of decreased V-ATPase activity in XMEA, we predicted that XMEA cells have elevated lysosomal pH and a resultant partial block in the common final degradative stage of autophagy. To test this, we first measured lysosomal pH. We incubated fibroblasts with Oregon green dextran overnight, during which dextran is endocytosed to the lysosome where it fluoresces with an intensity proportional to pH and emits two wavelengths around an isobestic point; fluorescence intensity at one wavelength is inversely proportional to the intensity at the other and their ratio corrects for focal plane artifacts (Supplemental Fig. 8) [26]. pH of patient lysosomes was 0.5 units higher (pH 5.2 vs. 4.7), i.e., three times less $[H^+]$, than that of controls (Fig. 6a). Next, we measured autophagy, by quantifying the degradation of long-lived proteins. We cultured lymphoblasts and fibroblasts for 48 h with radioactive cysteine and methionine. After washing, we chased protein degradation by measuring the TCA soluble fraction of total radioactivity for 72 h. Three types of chase media were used for the calculation of total autophagy, macroautophagy, and non-macro autophagy: routine media, media with lysosomal protease inhibitors (NH_4Cl and leupeptin), and media containing 3-methyl

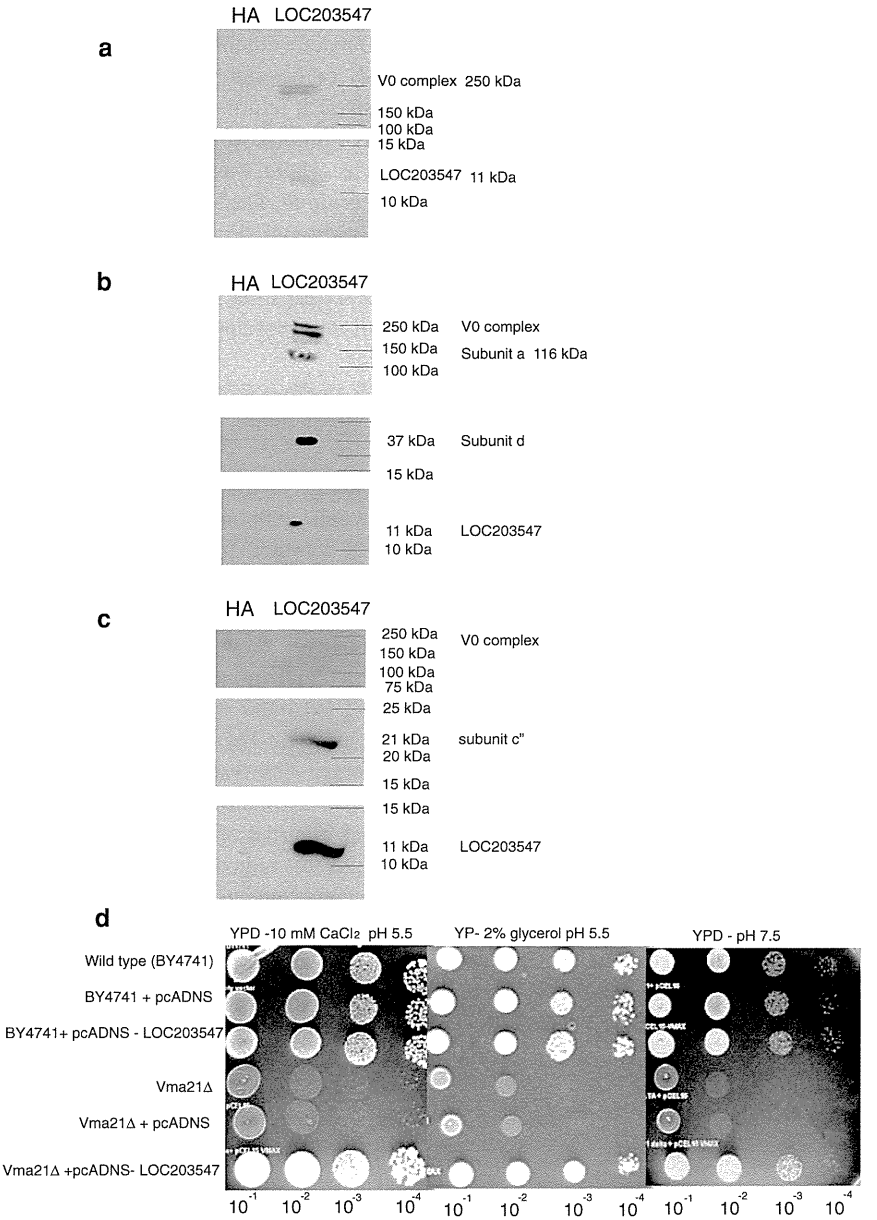

Fig. 4 LOC203547 interacts with V_0 via c", and LOC203547 rescues yeast *vma21Δ*. **a** LOC203547 antibody co-precipitates V_0 under non-denaturing conditions. Proteins from HEK293 cells solubilized in the presence of detergent C12E9 and DTSSP crosslinking were immunoprecipitated using an anti-LOC203547 antibody. The Western blot probed with anti-a antibody reveals the 250 kDa complete V_0, indicating that LOC203547 interacts with V_0. Subunit a is the dominant V_0 subunit (Supplemental Fig. 1). In yeast, V_0 assembly does not involve an initial interaction of Vma21p with subunit a, and Vma21p antibodies do not co-precipitate a except as part of intact V_0 (2). Absence of a 116 kDa band (subunit a) indicates that LOC203547 likewise does not separately interact with a. **b** When immunoprecipitation with the LOC203547 antibody was repeated in the presence of C12E9 but no crosslinking, the 250 kDa V_0 complex and subunits a (116 kDa) and d (37 kDa) were detected. Under these conditions, some amounts of at least these two subunits separates from the complex during SDS-PAGE, enabling their detection. **c** Under full denaturing conditions (no C12E9 and DTSSP crosslinking), immunoprecipitation using LOC203547 antibody and western blot using an antibody that recognizes both subunits c and c" detects only the 21 kDa c" subunit, no 250 kDa V_0 band, and no 16 kDa band corresponding to subunit c. **d** Comparison of growth patterns of yeast strains BY4741 (wild-type), *vma21Δ*, LOC203547-transformed *vma21Δ*, and controls. Successive dilutions (10^{-1}-10^{-4}) of synchronously grown cultures of each strain plated in three different growth media. LOC203547 rescues the *vma21Δ* growth defect

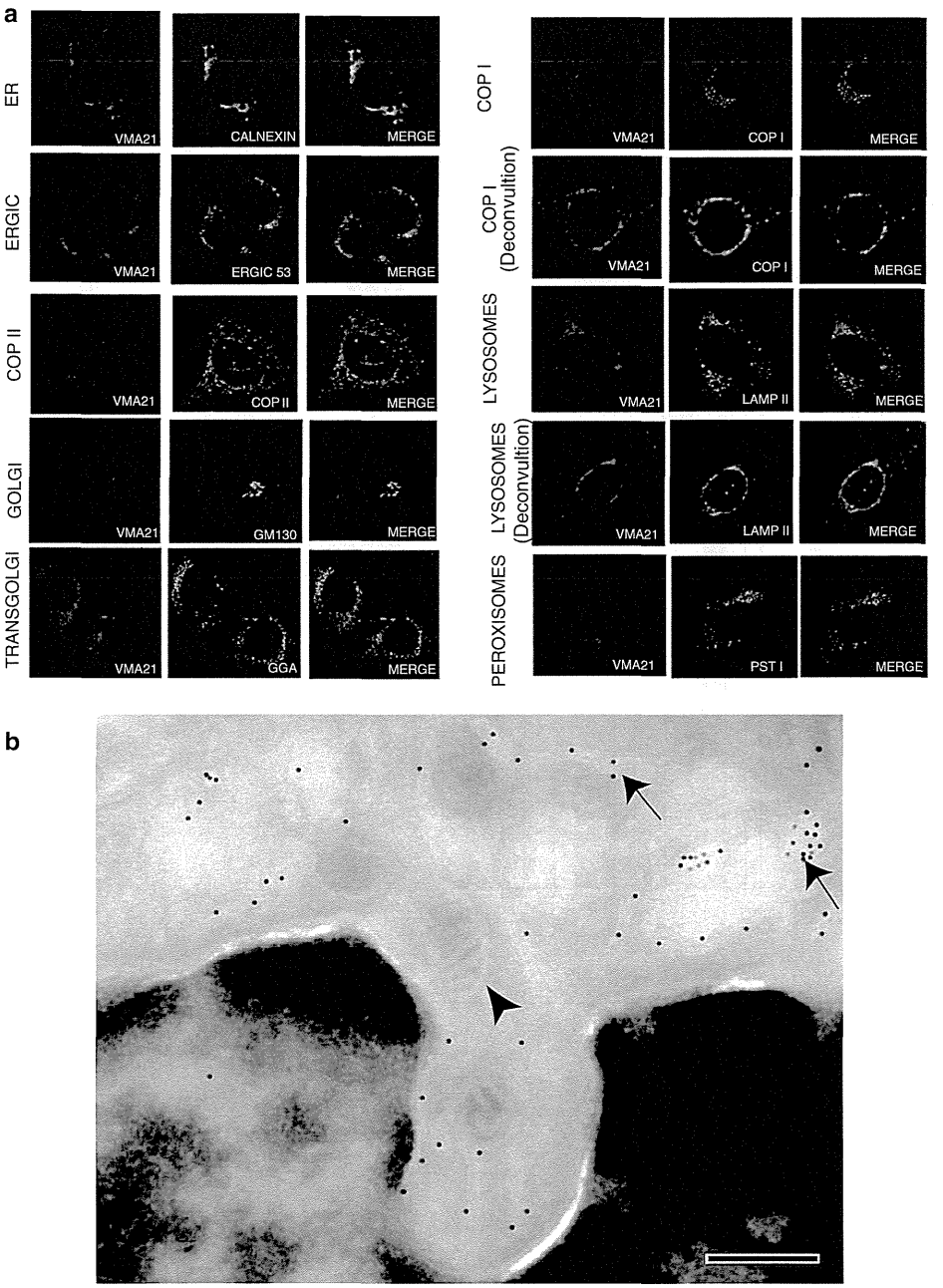

Fig. 5 Intracellular localization of VMA21. **a** Human fibroblasts were treated with VMA21 antibody and co-stained with antibodies against compartment-specific markers. *Yellow fluorescence* indicates co-localization. Standard confocal and deconvolution microscopy were performed. The former is shown for all structures. Deconvolution microscopy, which reduces false co-localization in situations of highly abundant signal, as was the case for lysosomes (LAMP2) and COPI vesicles, is also shown for the latter two compartments. VMA21 localizes at the ER, the ERGIC, and on COPII vesicles. **b** Electron micrograph of VMA21 immunogold labeled ultrathin cryosection of a C2C12 cell. Note the *black dots* (*gold particles*) at the ER (*upper arrow*) and ER terminal cisternae (*lower arrow*) but not on mitochondrion (*arrowhead*); *Bar* 0.25 μm

adenine, a specific macroautophagy inhibitor. We found that in controls and patients approximately half of long-lived protein degradation was macroautophagic and half through non-macro autophagy, that total long-lived protein degradation in patients was reduced by 25–50 % compared to controls, and that this reduction in autophagic flux was due approximately equally to reductions in macro and non-macro autophagies (Fig. 6b–d). Consistent with impaired macroautophagy, EGFR and p62, specific macroautophagy substrate proteins, accumulated in patient cells (Fig. 6e). In separate experiments, proteolysis of short-lived proteins, which is largely non-lysosomal, was unaffected (not shown). We reasoned that a block in the final degradative stage of autophagy might induce a feedback upregulation of macroautophagy, i.e., increased autophagic signaling and increased autophagosome formation to overcome the end degradative block. Beclin-1 is a pivotal early component of autophagic signaling; its increase and increased interaction with the class III PI3 kinase hVps34 leads to activation and upregulation of the macroautophagy

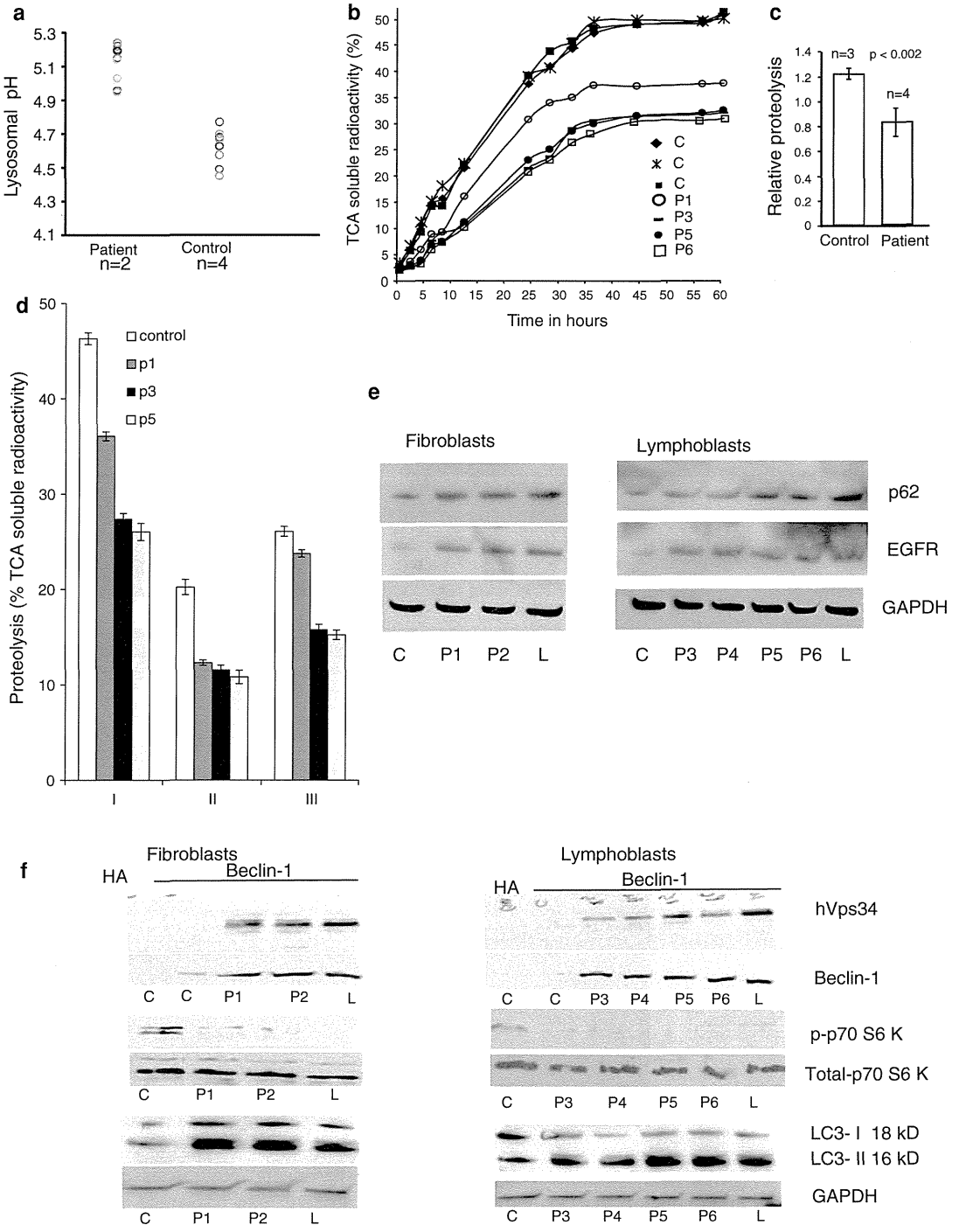

pathway [4]. LC3 is a cytosolic protein which upon activation of macroautophagy converts from its LC3-I (18 kDa) to its LC3-II (16 kDa) form to function in the isolation membrane that forms the autophagosome [21]. Western blot and immunoprecipitation studies in fibroblasts and lymphoblasts showed major increases in beclin-1, beclin-1-hVps34 interaction, and LC3-II in XMEA patients (Fig. 6f). LC3 was also increased at the transcriptional level, two-fold. The mRNA of a second early macroautophagy gene tested, *ATG12*, was increased ten-fold (Supplemental Fig. 9a). These results confirm that macroautophagy is upregulated in XMEA. We then tested the phosphorylation state of the p70S6 kinase and found it to be dephosphorylated (Fig. 6f) indicating that the

◀**Fig. 6** Increased lysosomal pH, decreased protein degradation, and increased macroautophagy. **a** Spread of lysosomal pH values in patient and control fibroblasts; each small circle is the mean pH measurement of 10 lysosomes per cell. **b** Chase of lysosome-dependent long-lived protein degradation in lymphoblasts. **c** Average rates of proteolysis in patients determined by calculation of slopes of the linear phases in (**b**) and expressed relative to control samples. *Error bars* show standard deviation, and *p* values were calculated using *t* Test. **d I**, 36-hour time points from panel b. **II**, Cells cultured with macroautophagy inhibitor 3-MA, measures non-macroautophagic portion of lysosome-dependent proteolysis. **III**, Difference between I and II, i.e., between total lysosome-dependent proteolysis and its non-macro autophagic portion; measures the macroautophagic portion. *Error bars* mean ± standard deviation of three independent repeats except for P5 bars II and III which are from two independent repeats. **e** Blocked degradative phase of macroautophagy in XMEA cells as evidenced by accumulation of the macroautophagy substrates EGFR and p62. Band intensities calculated using Image J: p62 in patient fibroblasts 0.48 ± 0.03 and 0.25 ± 0.008 in controls; EGFR in patient fibroblasts 0.277 ± 0.02 and 0.135 ± 0.009 in controls; p62 in patient lymphoblasts 0.45 ± 0.05 and 0.22 ± 0.07 in controls; EGFR in patient lymphoblasts 0.42 ± 0.02 and 0.14 ± 0.03 in controls. **f** Macroautophagic upregulation in XMEA cells (P1-P6) and low-dose leupeptin-treated non-XMEA cells (L); hVps34-beclin-1 interaction complexes were precipitated using a beclin-1 antibody followed by Western blotting for hVps34 and beclin-1: *Two upper panels*: both hVps34-beclin-1 are increased in patients and leupeptin-treated fibroblasts and lymphoblasts. Phosphorylation state of the p70S6 kinase determined by using phospho-specific (p-p70S6 K) and total p70S6 kinase antibodies: *Two middle panels*: p70S6 kinase is hypophosphorylated in patients and leupeptin-treated cells while the total p70S6 kinase levels remain similar. The mean intensities of p-p70 S6 K bands in fibroblasts: patients 0.060 ± 0.005 and controls 0.433 ± 0.010; in lymphoblasts: patients 0.149 ± 0.07 and controls: 1.04 ± 0.07; *Two lower panels:* Immunoblot of LC3: LC3-II concentrations are increased in patients and leupeptin-treated cells. Mean LC3-II: GAPDH band intensity ratios measured using Image J: 1.42 in patient vs. 0.17 in control fibroblasts. 0.707 in patient versus 0 0.079 in control lymphoblasts. LC3 mRNA quantifications are shown in Supplemental Fig. 9a, and LC3 immunocytochemistry in Supplemental Fig. 9b

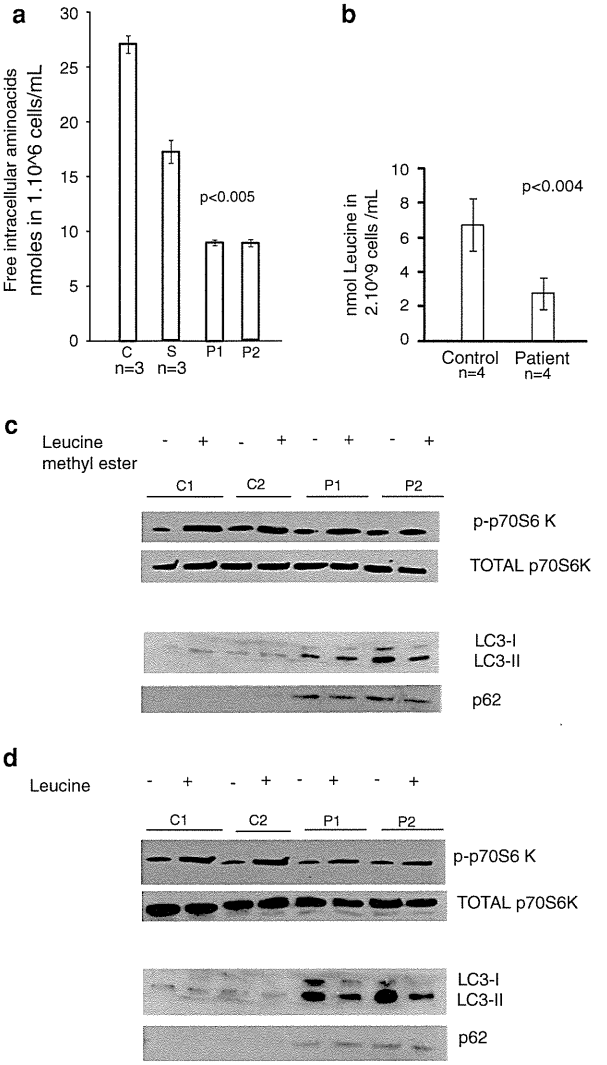

Fig. 7 Decreased intracellular amino acids and correction of autophagic upregulation by leucine esters. **a** Quantitation of intracellular free amino acids; *C* control fibroblasts; *S* control fibroblasts in starvation condition (Hanks balanced salt solution for 4 h); C and S are pooled results from three separate fibroblast lines each measured three times. Note, XMEA cells maintain themselves at even lower free amino acid concentration than the starved control cells. *Error bars* mean ± standard error on triplicate readings. **b** Quantitation of intracellular leucine in control ($n = 4$) and patient ($n = 4$) fibroblasts using LC–MS. *Error bars* show standard deviation from three independent repeats. **c** Phosphorylation status of p70S6 kinase is restored in patients treated with leucine methyl ester. **d** Phosphorylation status of p70S6 kinase is partially restored in patient cells treated with leucine

mTORC1 pathway is inhibited, and that the XMEA autophagic upregulation is at least in part through mTORC1 inhibition.

The mTORC1 pathway is chiefly inhibited (i.e., autophagy is activated) by reduced levels of cellular amino acids [1], which we measured and found to be ~50 % lower in XMEA than in control fibroblasts (Fig. 7a). Leucine is the principal amino acid involved in mTORC1 regulation [1, 2]. We measured its level specifically and found it reduced by over 50 % (Fig. 7b). Finally, supplementing the media with 10X leucine methyl ester (final concentration of 0.05 mM), a form of leucine that diffuses freely into cells [38], corrected the p70S6 kinase phosphorylation (Fig. 7c). Together, these results indicate that reduced cellular amino acids are at least in part the cause of autophagic activation in XMEA. Interestingly, while supplementing the media with normal leucine also corrected the phosphorylation status of the p70S6 kinase (Fig. 7d), it did not do so to the level of normal cells suggesting that leucine transport is decreased in XMEA, which, we hypothesize, is likely physiologic (see "Discussion").

Autolysosomes are evanescent structures that rapidly degrade their contents, and few are observed in normal cells at any one time. We asked whether in XMEA the upregulation of macroautophagy, coupled with delayed

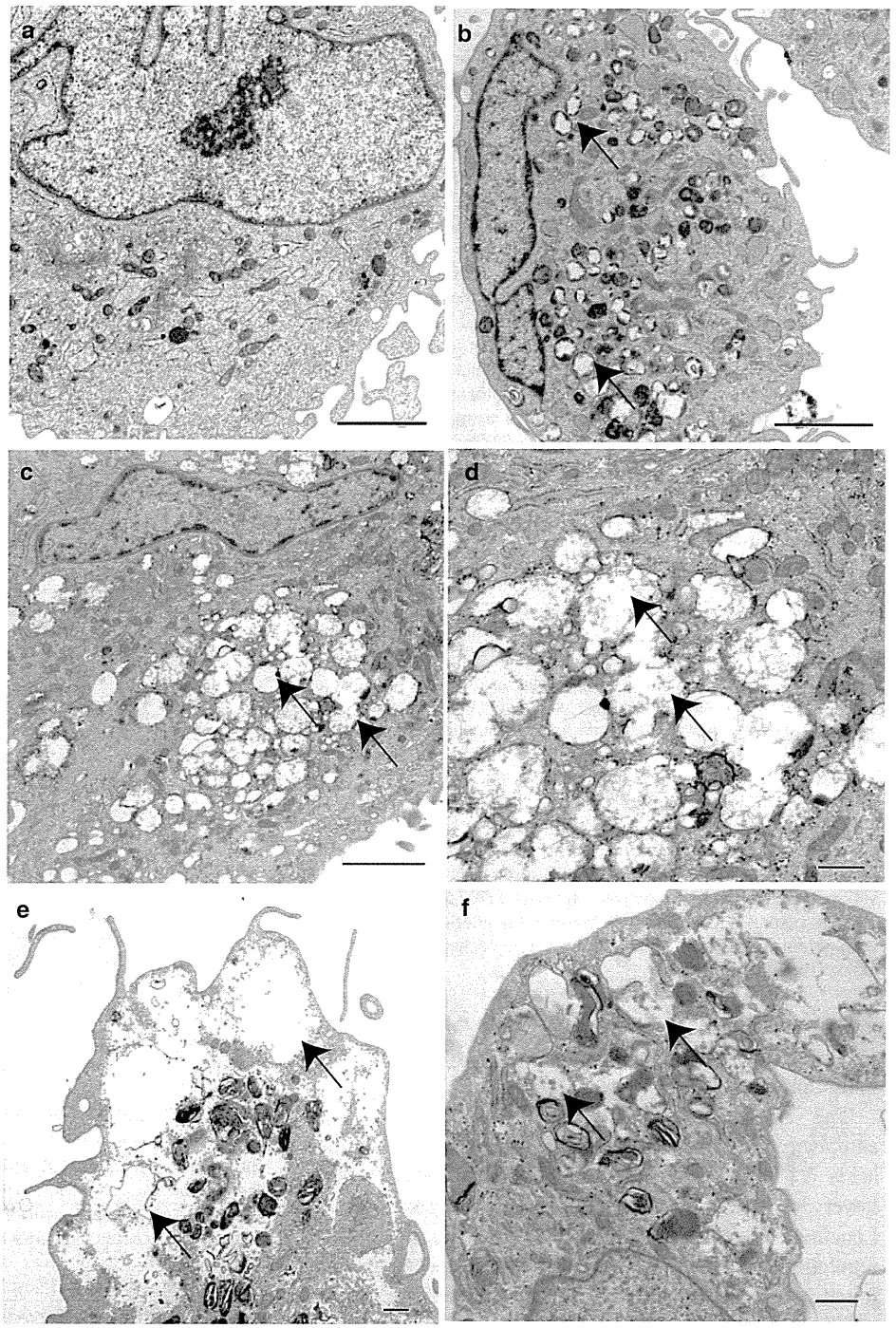

Fig. 8 Morphological Features of XMEA Fibroblasts (see also Supplemental Fig. 8). **a** Fibroblast from an unaffected individual; *bar* 2 μm. **b** Representative example of the most common appearance in patient fibroblasts; extensive number of autolysosomes distributed throughout the cell; *bar* 2 μm. **c** Autolysosomes in a fibroblast from an affected individual merging to form autophagic vacuoles. This was noted in 11 of 100 consecutive fibroblasts examined from two patients; bar, 2 μm. **d** Higher power of (C); *bar* 0.5 μm. **e** Extreme example of giant autophagic vacuolation in a fibroblast from an affected patient; *bar* 0.5 μm. **f** Representative non-XMEA normal fibroblast treated with leupeptin exhibits the morphological characteristics of XMEA; *bar* 0.5 μm

degradation of autolysosomal contents, results in increased autolysosomes. Electron and immunofluorescence microscopy showed a proliferation of autolysosomes in XMEA lymphoblasts, fibroblasts, leukocytes, and platelets (examples from fibroblasts shown in Fig. 8 and Supplemental Figs. 2g, 10). Cells were otherwise morphologically normal, except in a minority, counted at ~10 % in fibroblasts, where the numerous autolysosomes were observed merging one with the other forming large vacuoles comparable to the disease-defining autophagic vacuolation of XMEA skeletal muscle (Fig. 8c–e). These observations show that cells other than muscle also exhibit autophagic vacuolation in XMEA, although seemingly in lesser proportions (10 % in fibroblasts, present study, vs.

40–80 % in skeletal muscle [12, 36]). Further, the electron micrograph data is consistent with a progression from upregulated autophagy to proliferation of autolysosomes and finally to autophagic vacuolation.

We aimed to determine whether VMA21 mutations cause the above succession of events through the block in the final degradative stage of autophagy, and not through a separate mechanism, i.e., we asked whether blocking the degradative stage by 25–50 %, alone, elicits macroautophagy, and autophagic vacuolation. Leupeptin is a pH-independent inhibitor of lysosomal hydrolases and, therefore, of the degradative stage of autophagy. First, we determined 30 μM as the leupeptin concentration needed to decrease long-lived protein degradation by 37 % (Supplemental Fig. 11). Lymphoblasts and fibroblasts from normal subjects incubated with this concentration of leupeptin exhibited decreased mTORC1 dependent upregulation of autophagic signaling (Fig. 6f), and autolysosome proliferation, autolysosome mergers, and autophagic vacuolation (Fig. 8f), similar to XMEA.

Restoring VMA21 mRNA levels corrects the XMEA autophagic disturbance

As final proofs that decreased *VMA21* is the cause of the autophagic disturbance in XMEA, we performed the following experiments. We reduced *Vma21* mRNA in NIH 3T3 cells by silencing with *Vma21* RNAi and observed appearance of the typical XMEA vacuolation (Fig. 9a, b). Next, we raised the levels of *Vma21* mRNA in XMEA fibroblasts by retroviral infection and stable expression of *Vma21*. This led to near-normalization of V-ATPase at protein level (Fig. 9c), its assembly (as shown by near-normalization of free cytosolic subunit E (Fig. 9d), V-ATPase activity (Fig. 9e), and lysosomal pH (not shown). As a consequence, there were improvements in long-lived protein degradation, LC3 isoform levels, beclin-1 levels, beclin-1-hVps34 interaction, and intracellular amino acid levels (Fig. 9f–i). Autolysosomes and autophagic vacuoles were no longer present and cells returned to normal morphology (Fig. 9j).

Not all V-ATPase dependent functions are affected in XMEA

Multiple cell functions other than autophagy require the V-ATPase, none of which appear to be affected to a clinical extent in our patients. We studied one of these systems, maturation of lysosomal enzymes which consists of stepwise proteolytic processing in compartments with decreasing pH set by increasing V-ATPase activity [32]. We examined hexosaminidases A and B and cathepsin D in XMEA fibroblasts, and found that maturation of all three, as determined by polypeptide processing and in vitro activities, were identical to controls (Supplemental Fig. 12).

Discussion

XMEA mutations are hypomorphic alleles that reduce the amount of VMA21, in most cases by decreasing mRNA splicing efficiency. Only skeletal muscle is clinically affected and only in males. Female carriers are unaffected likely because muscle is a syncytium and half the nuclei will produce normal *VMA21* mRNA amounts. We show that VMA21 is the human ortholog of the yeast V-ATPase chaperone Vma21p, and that reduced VMA21 results in reduced V-ATPase activity to 10–30 % of normal. The human proteome lacks the c' V-ATPase subunit with which the yeast Vma21p interacts. We find that human VMA21 interfaces with the V-ATPase through the c" subunit, although it may well have additional contacts. VMA21 may also have functions other than assembling the V-ATPase, mediated through other interacting partners.

Several other genetic diseases affecting V-ATPases have been described. In these diseases, mutations affect particular V-ATPase subunits that confer subcellular location or tissue specificity and result in corresponding symptoms such as developmental delay with wrinkled skin syndrome (subunit a2) [14], osteopetrosis (subunit a3) [9], and renal tubular acidosis with deafness (subunit a4) [13]. XMEA is the first disease in which all V-ATPases are affected. On the other hand, XMEA mutations do not completely eliminate V-ATPase activity. XMEA patients do not exhibit neurodevelopmental delay or clinically manifest skin and bone abnormalities, acidosis, or hearing loss, indicating that for the specialized a2, a3, and a4-containing V-ATPases, the reduced V-ATPase assembly in XMEA does not reach clinical threshold.

The reduced V-ATPase activity in XMEA results in a rise in lysosomal pH from 4.7 to 5.2. Maturations and activities of three lysosomal enzymes tested are not affected in vitro. However, in vivo, these enzymes are expected to have lowered activity in patient lysosomes due to the raised pH. Hexosaminidase, e.g., is known to be 50 % less active at pH 5.2 than at 4.7 [32]. Not surprisingly, this degree of hexosaminidase downregulation is tolerated by XMEA patients because they, like Tay-Sachs disease carriers who also have 50 % reduced hexosaminidase, do not have Tay-Sachs symptoms. Other individual lysosomal enzymes are likely similarly subclinically affected.

The final stage of autophagy, i.e., the collective activity of lysosomal enzymes involved in the degradation of long-lived proteins, is also reduced. The extent of this reduction in patient cell lines is certainly greater than the 50 % we recorded, because, as we showed, it is coupled with a